4

Combined metagratings for efficient broad-angle scattering metasurface

Ich will einen Sommer lang nur tanzen

Einen Sommer lang nur tanzen – Fiva

Spectrally controlled diffusion and reflection of light are key operations for light management in many optical devices. Integration of this operation in complex nanophotonic devices requires a 2D interface that provides tailored spectrum and directivity control. Here, we present a metagrating superstructure that realizes a resonant light reflector with tailored angular scattering profile. Millimeter-sized metasurfaces are built from arrays of combined supercells of 20-50 μm, composed of 5-7 differently pitched metagratings that tailor at will and with large efficiency the angular response. Each supercell is composed of one or more Si Mie resonators, arranged in a periodic array above a Ag back plane and tailored to resonantly scatter light at 650 nm into only the ±1 diffraction orders with very high efficiency. By varying the pitch and supercell design, we can tailor the overall metasurface reflection profile with large flexibility, realizing a broad-angle Lambertian-type scattering metasurface, as well as a large-angle (35-75°) scattering metasurface, both with resonant optical scattering efficiencies above 70%. These ultra-thin structures, fabricated using thin-film deposition, electron beam lithography and reactive ion etching, can find applications for light trapping and spectrum splitting in solar cells and other devices.

4.1. Introduction

Materials to control light diffusion are traditionally composed of randomly packed high-index particles that support multi-wavelength scattering. These materials are typically based on multiple random scattering events, and therefore need to have thicknesses much larger than the optical wavelength. The properties of random media used for light scattering in solar cells [55, 56], random lasing [57, 58] and investigation of Anderson localization [59, 60] have been intensively studied. Random media often used in these studies consist of various types of "white paint"[55–57]. Artificially made random media for light diffusion such as photonic glass [58] and Mie glass,[61] have also been demonstrated.

For various applications, it is important to have randomly scattering devices with a much smaller thickness. In recent years, the metasurface literature has offered different solutions for flat two-dimensional surfaces providing diffuse scattering. So far, these solutions have been based on phase-coded metasurfaces, engineered by distributing a limited number of inclusions in a random-like fashion to locally manipulate the phase, amplitude and polarization of light, and thereby the shape of the scattered wavefront. Some work has been done on phase-coded metasurfaces for diffuse-like scattering with quasi-random phase coding in the microwave and infrared regime[62–64]. Metasurface diffusers at optical wavelengths were also studied, and their far-field response and performance for speckle-free imaging was studied[65–67]. However, graded metasurfaces composed of passive scattering surfaces have a fundamentally limited beam bending efficiency[68–70].

In this work, we demonstrate efficient broad-angle and large-angle light scattering from metagratings formed by locally periodic arrays of carefully tailored inclusions above a reflecting backplane, applying and extending a rigorous analytical theory that was introduced by Ra'di et al.[71]. In the optical spectral range, a metagrating is composed of resonantly scattering plasmonic or Mie particles placed in a periodic array above a metal reflector, supporting a discrete set of grating orders. For a well-chosen scattering cross section and spacing between scatterers and reflector, the specular reflection at resonance is fully cancelled by destructive interference of reflection from the back mirror and the zeroth order Floquet scattering mode[71]. In addition, the resonant scatterer geometry can be designed to only allow scattering power in one desired diffraction order, and to completely suppress scattering into all other allowed orders. Metagratings can be designed to operate around a resonant wavelength, with a tailored angular scattering profile, and an efficiency that is fundamentally limited only by absorption in the involved materials[71]. They can operate using either magnetic[71] or electric resonant modes[72]. Freeform inverse designs and fully analytical schemes to design metagratings employing diffraction gratings have been investigated[73–75]. This concept has also been employed to tailor wavefront control in transmission and reflection[76–78] using optimized scatterers with a shaped emission profile, without a direct link with theory.

Here we design a metasurface that combines multiple metagratings with different periodicities placed side by side in a supercell to create a reflector with precisely-engineered scattering profile. We extend the metagrating theory[71] and use numerical optimization to create a design based on magnetic Mie modes, experimentally demonstrating the functionality of the combined metagratings. A key feature of the proposed metasur-

face design is that it relies on a well-defined and precisely-engineered scattering profile, in contrast to most random light scattering geometries based on multiple scattering.

The reflecting metasurface presented here is composed of five characteristic length scales, designed based on the following steps (see Figure 4.1): (a) Si nanoparticles are designed to have a magnetic Mie resonance in the red spectral range; (b) the unit cells are composed of one or, in part of the structure, multiple scatterers to tailor angular scattering; (c) these unit cells are then placed in periodic arrays above a Ag backplane to form a metagrating that scatters light to a single diffraction order; (d) multiple metagratings are arranged into a supercell composed of 7 differently pitched metagratings to create a supercell with tailored angular scattering distribution; (e) a full-scale metasurface sample is then built up from randomly placed supercells.

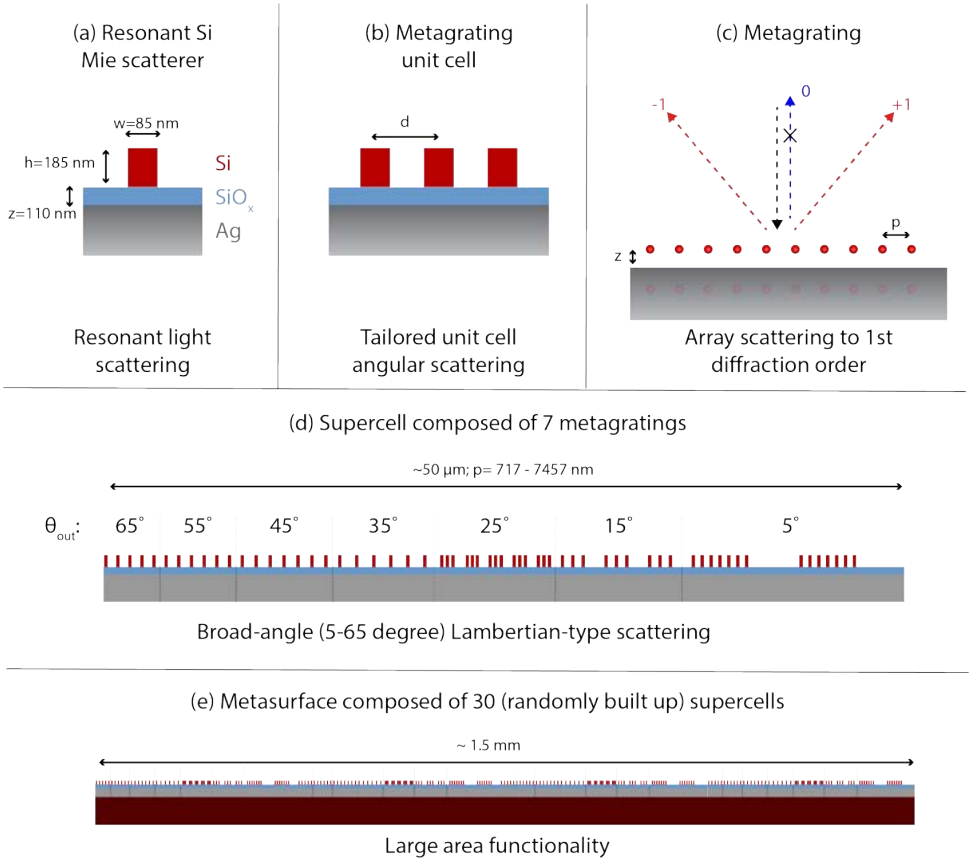

Figure 4.1: Metasurface design and length scales. Unit cells composed of one or more Si Mie resonators are arranged in a periodic array placed above a metal back plane to form a metagrating that scatters into only the ±1 diffraction orders. A supercell of metagratings creates a tailored angular response, and an array of supercells forms the large-area macroscopic metasurface.

Resonant broad-angle scattering profiles with well-defined angular distribution can find applications as diffusors, approaching a Lambertian scatterer. For example, reso-

nant diffusers can enable the creation of a matt appearance effectively creating "nanostructured paint", which has applications in e.g. colored solar cells [24, 25]. Creating structural color using dielectric nanoparticles[44–46] has been demonstrated before, focusing on spectral control rather than spectral and directivity control. To demonstrate the versatility of the metagrating design, we also demonstrate a functional surface with tailored large-angle scattering profile. This structure overcomes the typical inefficiencies faced by structures designed to scatter energy towards very large angles and can improve light trapping and spectrum splitting in (tandem) solar cells.

4.2. Theory and design

Following the work of Ra'di et al.[71], we first design a metasurface composed of an array of horizontally oriented magnetic dipoles located at a distance h above a perfect electrical conductor [see schematic in Figure 4.2 (a)]. Here, we consider normally incident light and set the periodicity in order to support two symmetric diffraction orders (i.e., ±1). The distance h can be controlled so that the fields in the specular direction are fully cancelled by destructive interference of light reflected from the mirror and the resonantly scattered zeroth-order Floquet grating mode. In this geometry all light can be redirected to a single desired diffraction order (+1 or -1) by choosing the resonant scatterer geometry, in such a way that scattering into the other diffraction order is nullified. Here since we aim at a symmetric angular scattering profile, we will design the metagrating to equally scatter into symmetrically-directed +1 and -1 channels.

Throughout the chapter, we limit the calculation and experiments to 2D functionality under normal incidence, however the same concepts can be readily extended to 3D and to any incoming illumination angle. The magnetic dipoles, induced by the incoming transverse magnetic (TM) plane wave $E_{inc} = E_0 \mathbf{y} e^{-ik_0 z}$ with amplitude E_0 and free-space wave number k_0, form a magnetic current $I_m^x = -i\omega\alpha_m H_{ext}^x$ where ω is the angular frequency, H_{ext}^x is the local magnetic field at the location of the particle, sum of the incident field and the reaction from the array, and α_m is the effective magnetic polarizability, including the array coupling. As shown earlier [71] (see also the analytical derivation in the Supplementary Material), α_m satisfies the generalized passivity condition

$$Im\left(\frac{1}{\alpha_m}\right) = \frac{\omega}{\eta_0 d}\sum_{n=-\infty}^{n=+\infty}\frac{1}{\cos\theta_n}\cos^2(k_0 h\cos(\theta_n)) \tag{4.1}$$

with η_0 being the free-space wave impedance, d the periodicity in the y direction and θ_n the diffraction angle(s) given by the grating equation. For normal-incident light, the zeroth order Floquet mode of the radiated field is $\boldsymbol{E_0} = Q_0 \boldsymbol{y} e^{-ik_0 z}$, where $Q_0 = \frac{1}{d} I_m^x \cos(k_0 h)$. The direct reflection from the ground plane can be cancelled by the Floquet mode if $Q_0 = E_0$. This leads to the following condition:

$$\frac{1}{\alpha_m} = \frac{2i\omega}{\eta_0 d}\cos^2(k_0 h) \tag{4.2}$$

For a grating with ±1 grating orders, equation 4.1 and 4.2 lead to the design equation for the cancellation of specular reflection:

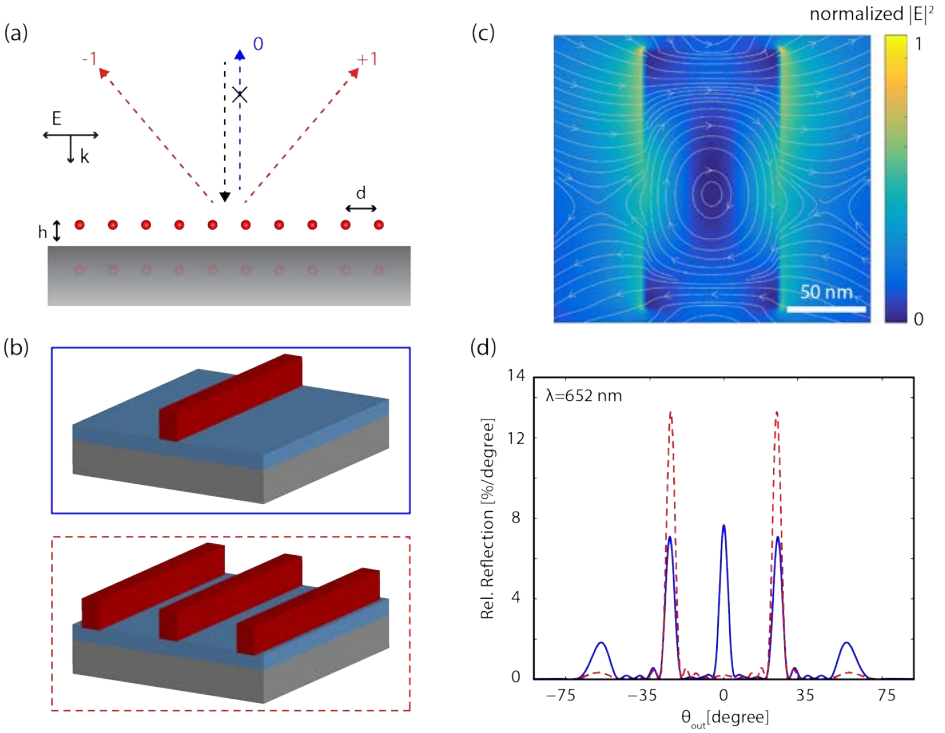

Figure 4.2: Magnetic dipole resonances in a 1D metagrating array (a) Periodic array of magnetic dipoles arranged over a ground plane. (b) Schematic of unit cells with one or three silicon bars on a silica spacer layer on top of a silver mirror. (c) Normalized electric field intensity $|E|^2$ and electric field lines (grey) in vertical crosscuts through an 85 nm wide and 180 nm tall Si bar on 110 nm SiO_x spacer layer on top of a silver mirror, parallel to the electric driving field. (d) Simulated angular scattering at λ = 652 nm in the far field for a finite metagrating with just 5 periods with pitch of 1538 nm. Unit cells are composed of a single silicon bar (solid blue line) or three silicon bars (spaced by 230 nm; dashed red line) placed above a Ag ground plane with a 110 nm silica spacer. Light coupling to the specular reflection and second order diffraction is suppressed for the three-particle unit cell.

$$\cos^2(k_0 h) = \frac{2}{\cos(\theta_1)} \cos^2(k_0 h \cos(\theta_1)) \tag{4.3}$$

Next, we create a metasurface that is composed by a distribution of metagratings, each designed to create a symmetric scattering profile over a different angular range. Given the limited size, each of them does not offer large directivity, but this is not an issue since the overall goal is to tailor the scattering over a broad angular range. By combining several of them placed next to each other, the overall scattering distribution can be tailored with large flexibility. In our design, we choose angles in a step size of 10°, to fill a major part of the scattering profile while maintaining the lateral dimension of the metasurface supercell below 100 µm.

4.3. Broad-angle scattering metasurface

4.3.1. Numerical simulations

2D Finite-Difference Time Domain (FDTD) simulations were performed to design a broad-angle scattering metasurface with engineered scattering profile. The unit cells in each metagrating are composed of one or more silicon rods placed on top of a silver mirror with a silica spacing layer, surrounded by air, see Figure 4.2(b). Each Si rod has a width of 85 nm, a height of 180 nm and the silica spacing layer has a thickness of 110 nm. The parameters of the rod are kept constant in all parts of the structure as the performance does not improve substantially for the different metagratings with changing parameters. Details of the numerical optimization can be found in the Supplementary Information. The structure is excited by TM-polarized light at normal incidence. The normalized electrical field distribution for a single scatterer on the silica-covered silver mirror at the resonance wavelength λ = 665 nm is plotted in 4.2(c) and the field lines show the typical electrical field loop corresponding to a magnetic dipole [50]. A single supercell of the structure is composed of an array of metagratings that are each composed of 2 to 7 periodically placed unit cells, to steer light efficiently towards the desired angular range. The number of unit cells for each metagrating is indicated in the schematic of 4.1(c) and the dimensions of all parameters are listed in Table 1. Side-by-side metagratings are spaced by the distance of one of the periodicities. We aim the broad-angle metasurface to operate in the 0-65° angular range, with metagratings scattering from 5-65°. The scattering towards 0° is provided by the residual of the specular reflection, so no extra supercells are needed to cover this portion of the scattering spectrum.

To address angles below 30°, we could utilize conventional gradient metasurfaces that perform well for small angles [68]. Here, instead, to cover this angular range we extend the metagrating concept and design a surface that not only eliminates scattering into the specular direction, but also has zero scatterings into higher orders modes other than ±1, leaving only scattering into the first diffraction orders (i.e., ±1). To do so, we compose the metagrating unit cell (that needs a single scatterer in the case of large-angle deflection, as in the design described above) of either 3 or 6 of identical scatterers, with their lateral distance tuned to achieve a scattering angular distribution that mainly couples to the first-order diffraction angle. This new approach has two advantages compared to conventional gradient metasurfaces: first, by maintaining the symmetry in the unit cell, the scattering effect remains angularly symmetric, which is ideal for our operation, but not typical for gradient metasurfaces; second, the higher scattering cross section of the composite unit cell helps balance the reflection from the mirror with the resonant scattering, thereby suppressing more efficiently the specular reflection. 4.2(d) shows the simulated angular scattering in the far field at λ = 652 nm for a finite metagrating with 5 periods and a pitch of 1538 nm (see schematic in 4.2(b)), composed of Si cylinders with dimensions described above. Clearly the three-particle design reduces the specular reflection, as well as higher-order diffraction in the metagrating geometry. This extension of the metagrating design, in which multi-particle resonant scattering and grating diffraction are combined, creates a tailored angular scattering distribution over a broad angular range that covers both small and large angles. According to Eqn 4.3, the optimum spacing h to cancel specular reflection increases for larger grating pitch. For the ease of fabrication, the silica spacing layer was kept constant for all metagratings

and optimized for diffraction towards 35°.

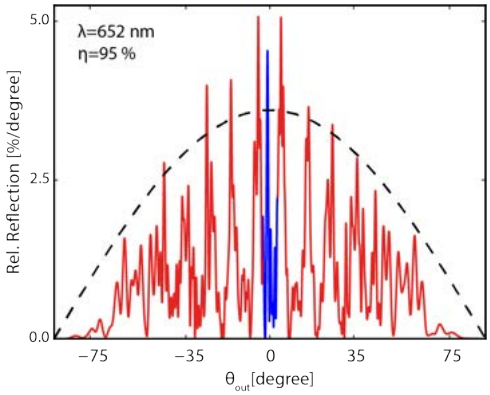

Figure 4.3: Broad-angle metasurface. Simulated angular scattering at $\lambda = 652$ nm in the far field for the broad-angle metasurface illuminated at normal incidence composed of diffracted (red) and specularly reflected (blue) light. The dashed black line shows the angular profile of a perfect Lambertian diffusor.

4.3 shows FDTD simulations of the far-field intensity of light reflected off our optimized design for a broad-angle metasurface at an operational wavelength of $\lambda = 652$ nm. Detailed dimension of all elements in the full metasurface design are given in Table 4.1. The metasurface supercell is composed of 7 metagratings with unit cells composed of either 1, 3, or 6 Si bars placed side by side (see 4.1). The number of unit cells in each metagrating was chosen such that the scattering intensity follows a Lambertian cosine distribution. In Figure 4.3 the effect of the distinct metagratings is seen in the discrete peaks in the scattering profile, and the overall shape follows the trend of a Lambertian profile that is overlaid for reference. We find that in this design the specular reflection is nearly fully eliminated, higher-order modes are effectively suppressed, and 95% of the incident light is scattered into the desired angular range. We note that in our simulations the scattered distribution is composed of discrete peaks. These are expected to be readily smeared out to create a smooth distribution by expanding the metagrating size and tailoring the range of metagrating pitches. In practical applications in photovoltaics the maximum number of metagratings in a unit cell is determined by the coherence length of sunlight. Importantly, the angular distribution will smoothen out when a broader spectral bandwidth of excitation is considered.

4.3.2. Experiment

Thin layers of silver (200 nm), SiO_x (110 nm) and silicon (185 nm) were deposited successively on a Si substrate by electron-beam thin-film deposition (Polyteknik Flextura Evaporator). After deposition, a 40 nm layer of HSQ was spin-coated on top of the silicon (Suss Microtec Delta 80 spincoater), patterned by electron beam lithography (Raith Voyager 50 kV electron beam lithography system) and developed in TMAH at 50 °C for 1 minute. After development, the rod geometry was transferred from the HSQ mask into the silicon using reactive ion etching (RIE) in a HBr_2 (48.5 sccm) and O_2 (1.5 sccm) plasma (Oxford PlasmaPro100 Cobra). The SiOx layer serves as an effective etch stop. The surface was

Parameter	Symbol	Broad-angle metasurface	Large-angle metasurface
Si Mie scatterer width	w	85 nm	85 nm
Si Mie scatterer height	z	180 nm	180 nm
Silica spacer layer thickness	t	110 nm	110 nm
Spacing between Mie scatterers and Ag mirror	h	200 nm	200 nm
Number of Mie resonators/ spacing in unit cell	n/d	6 /230 nm (5°) 3 /470 nm (15°) 3 /550 nm (25°) 1 (>25°)	1
Grating pitch in metasurface	p	720 nm (65°)- 7500 nm (5°)	670 nm (75°)- 1130 nm (35°)
Number of metagratings in supercell	-	5	7
Size of supercell	-	50 mm	20 mm
Spacing between supercells	-	720 nm - 7500 nm	670 nm - 1130 nm
Total metasurface size	-	1.5×1.5 mm2	1.5×1.5 mm2

Table 4.1: Overview of design parameters for broad-sngle and large-angle metasurfaces

fabricated in a 1.5×1.5 mm^2 field. Figure 4.4 shows a cross-section secondary electron microscopy (SEM) image of a single Si rod and a top-view SEM image of the supercell composed of 7 different metagratings. To circumvent diffraction effects each supercell of the metasurface is composed of a different arrangement of the same 7 metagratings. The distance between the supercells is varied from 720 nm - 7500 nm. The exact parameters of the structure for the broad-angle metasurface is listed in Table 4.1.

Optical reflection spectra were measured using an integrating sphere setup with the sample tilted 8° relative to the incoming collimated beam from a broad-band light source, to capture all scattered and specularly reflected light from the surface in the integrating sphere. Additional scattering measurements were made capturing only scattering into the grating orders (i.e., without specular reflection). In this case, the sample was placed without tilt at the back side of the integrating sphere, so that specularly reflected light was reflected out through the entrance opening of the integrating sphere. Figure 4.4(b) shows the measured total reflection and scattering spectra of the broad-angle reflecting surface. A clear scattering peak is observed around 636 nm, demonstrating the Mie-resonant nature of the metagrating geometry. The total reflectivity of the surface in the measured spectral range is 60-80%, with the remainder of impinging light being absorbed in the Ag back reflector and in the Si bars. This expectation is confirmed by the resonant dip in the total reflectivity at resonance.

The measurement setup for the angle-resolved reflection measurement is shown in Figure 4.4(c). A collimated, p-polarized beam of 636 nm light is incident on the sample surface. A detector (collection solid angle 0.0015 sr) positioned on a rotating stage around the sample allows angle-resolved measurements. In order to measure the spec-

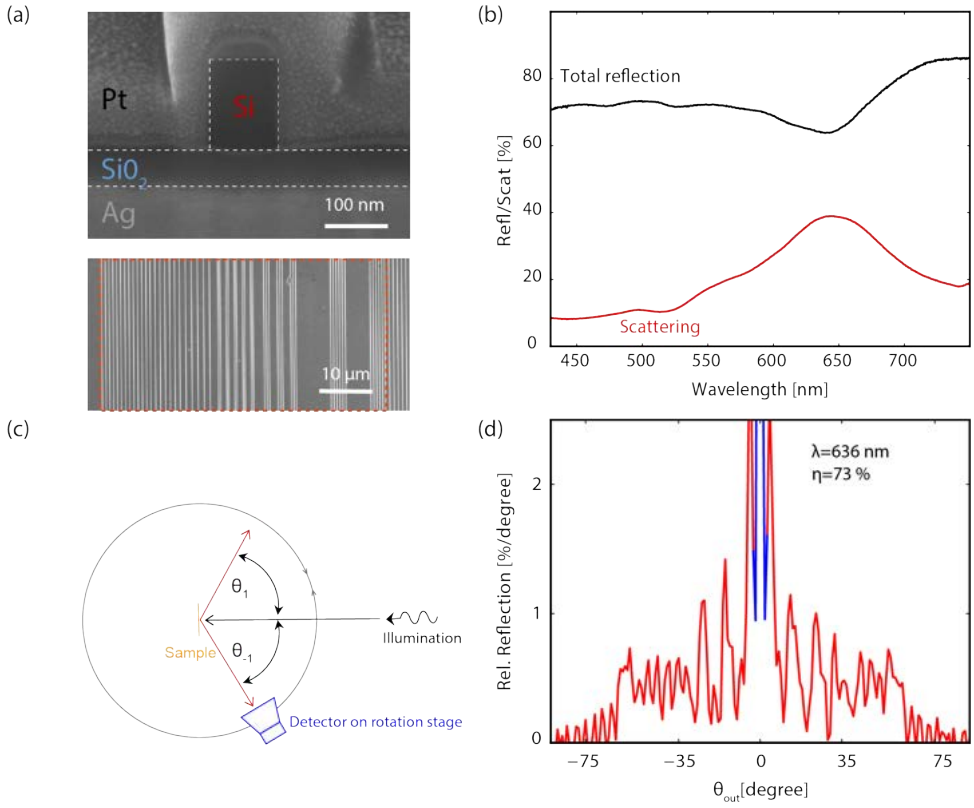

Figure 4.4: Fabricated broad-angle metasurface and optical measurements (a) top: Cross-section SEM image of a silicon bar on a SiO_x layer on Ag. To create image contrast the sample was covered with platinum before performing the FIB cross-section. Bottom: Top-view SEM image. The red dashed box represents a supercell composed of 7 differently pitched metagratings. (b) Total reflection (black) and scattering excluding specular reflection (red). (c) Schematic of angular scattering setup. The sample in the center of a rotating stage is illuminated with a vertical tilt of 10° by a collimated p-polarized light beam (spectral bandwidth 2.5-5 nm). The detector on the rotating stage with a vertical tilt of -10° collects the reflected power at a given horizontal angle θ_{out}. (d) Measured angular reflection on resonance (λ = 636 nm). The red data indicate the diffracted scattering, the blue data specular reflection.

ular reflection into the 0th order, the beam is incident under a vertical angle tilt of 10° above the sample and the detector is 10° below the sample. The angle-resolved measurement at the resonance wavelength [636 nm, bandwidth 2.5-5 nm, Fig. 4.4(d)] shows an overall spectral shape similar to simulations. In the experiment, 73% of the total reflected power is scattered into the 5-65° angular range. We attribute the remaining specular reflectivity (27%) to the fact that a fixed SiO_x thickness was used for all grating periods (while the optimum thickness decreases with pitch) and small fabrication inhomo-

geneities. The overall Lambertian shape can be approximated in experiments, but the specular reflection as well as small angle diffraction at 5 degrees does not follow exactly the calculated trend. These limitations can be attenuated by using an advanced metagrating fabrication procedure, to fully cancel the specular component. As mentioned earlier, the metagrating approach leads to a resonant behavior of the structure. Off-resonance, the metasurface shows very limited broad-angle scattering as is described below.

4.4. Large-angle reflector metasurface

4.4.1. Numerical simulation and experimental results

To illustrate the versatility of the metagrating design introduced here, which enables tailoring the angular scattering profile with large flexibility, we designed, fabricated and measured a scattering metasurface that only scatters into a predefined range of large angles. Such functionality is highly beneficial, for example, in light trapping applications in solar cells, where incident sunlight must be coupled to the in-plane waveguide modes of the solar cell [48, 79]. The large-angle scattering metasurface is composed of 5 metagratings that steer light into the 35-75° angular range, with each metagrating composed of 5 unit cells including a single silicon rod. Figure 4.5(a) shows the numerical simulation of the far-field angular scattering distribution of a single supercell [see Figure 4.5(b)] near the Mie-resonant wavelength at 660 nm. In this design, more than 90% of the incident power is scattered towards the ± 1 diffraction orders. An SEM top view of the fabricated large-angle metasurface is shown in Figure 4.5(c). The measured angular reflection [Figure 4.5(d)], shows the same trend as in simulations; 84% of the light is scattered into large-angle diffraction orders at resonance. The total reflection and scattering measurement data are shown in Figure 4.5(e), and clearly prove the resonant scattering nature of the large-angle metasurface.

4.4.2. Off-resonance optical performance of metasurfaces

As mentioned earlier, the metagrating design is based on resonant scattering from the building blocks. Figure 4.6 shows off-resonance (λ = 500 nm) reflection measurements of the broad-angle reflector and the large-angle reflector, overlaid with the resonant data presented above, i.e., Figures 4.4(d) and 4.5(d), respectively. The integrated off-resonance scattering efficiencies towards the grating orders are only 11% and 18% for two respective designs. This clearly shows that the proposed metagrating works on the principle of resonant scatterers. The existing off-resonance non-specular scattering of the structure can be explained by the broad linewidth of the magnetic dipole resonance of the silicon rods, as well as the existence of higher order modes that were not considered in the design.

A demonstration of the metagrating working as a “nanostructured paint” can be seen in Figure 4.7, which shows two photographs of the same sample, with 4 fields of broad-angle scattering metasurfaces in the left row and 4 fields of large angle scattering metasurfaces in the right row, respectively. The dimensions between the fields vary slightly due to a different choice of electron dose in the electron beam lithography writing. The SEM images and optical measurements of the two lowest fields are shown in this manuscript.

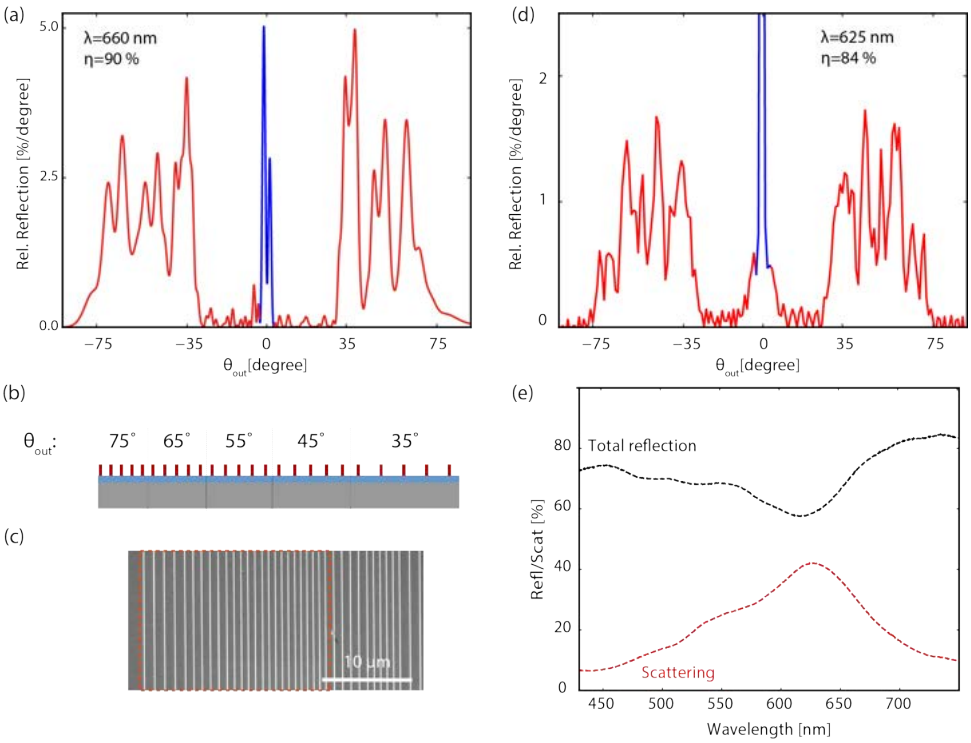

Figure 4.5: Large-angle reflector metasurface. (a) Numerical simulations of the angular reflection in far field for a single supercell of the large-angle reflector. (b) Schematic of the supercell. (c) SEM top view of the fabricated metasurface, the orange dashed box indicates a single supercell. (d) Angular reflection on resonance (λ = 625 nm). The red data indicate the diffracted scattering, the blue data specular reflection. (e) Total reflection (black) and scattering without specular reflection (red) of the large-angle reflector.

In both photos unpolarized white light is incident from the top, perpendicular to the sample. On the first photo, the specular reflection is captured by taking a photo from the top, in the second photo the scattering created by the metagratings is captured under an angle (around 45°). The color change visible in the photos indicates that only the color around the resonance (orange) is scattered sideways, and the rest of the spectrum (blueish, due to removed orange part of the spectrum) is reflected specularly.

4.5. Discussion and conclusions

In this work we demonstrated metasurfaces composed of combined metagratings with tailored angular scattering profiles. Based on a theoretical dipole scattering model, we

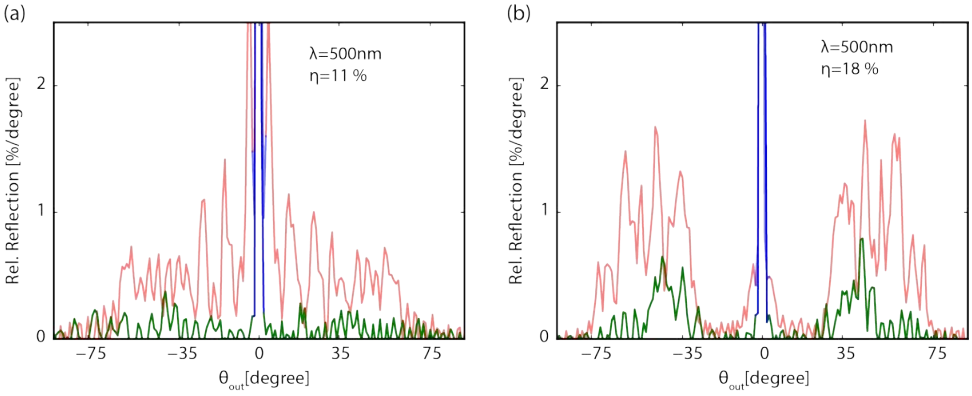

Figure 4.6: Measured angular reflection of the broad-angle reflector (a) and the large-angle reflector (b), off-resonance at λ = 500 nm. Diffracted scattering (green) and specular reflection (blue) contributions are shown. Data for resonant excitation (λ = 650 nm, same as Figure 4.4(d),4.5(d)) are overlaid for reference (red).

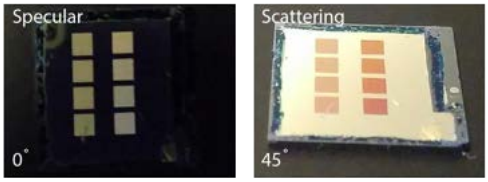

Figure 4.7: Photograph of sample with broad-angle scattering metasurfaces (left row) and large angle scattering metasurfaces (right row) illuminated by unpolarized white light under normal incidence. Photo taken under 0° (left) and 45° (right).

designed these ultrathin surfaces to realize broad-angle and large-angle scattering profiles. Using nanofabrication, we created Si Mie resonators on a Ag backplane and arranged the differently pitched metagratings in a supercell geometry to scatter light over the desired broad angular range. Combining multiple scatterers within a metagrating unit cell allows further control of the angular response, suppressing higher-order diffraction modes. Specular reflection is strongly suppressed, with 73% and 84% of the incident light scattered into the defined set of angles on resonance, for the broad-angle and large-angle geometries, respectively. Based on the same principles introduced here, extension of the design to 3D functionality and dual polarization can be readily explored. For example, 3D cylinders as scattering units have polarization independent resonance behavior and they could be placed in hexagonal grids to enable functionality on 3 axes. A further natural step for this work is to realize transparent resonant metagratings by controlling the interaction between suitable stacked Mie resonators, to replace the reflective back plane, in applications where transparency in the off-resonant spectral band is required.

Due to their high scattering efficiency and resonant operation, metagratings can

be used in a wide range of applications. The ultrathin resonant metastructures effectively create the functionality of "nanostructured paint", which can find applications in photovoltaics with colored appearance, a topic of great interest recently. By combining metasurfaces with different resonance wavelengths, multiple colored pixels may be envisioned, as well as diffuse surfaces with a white appearance [25]. Similarly, due to the spectral sensitivity, the presented metasurfaces can serve as spectrum splitting architectures in tandem solar cells. Furthermore, the large-angle scattering design can serve to enhance light trapping in thin-film solar cells, improving the effectiveness of coupling to in-plane waveguide modes. Many other applications in geometries that require a tailored (colored) scattering apperance come to mind as well, for example in controlling emission profiles in solid-state lighting and signaling where the spectral and directional control of light is important. The metagrating geometry introduced here, with many different length scales, can be readily fabricated in larger volumes using substrate conformal soft imprint lithography (SCIL)[38]. A full metagrating master pattern is then first made in a silicon wafer using electron beam lithography, from which a soft imprint stamp is then made that can transfers the pattern into a silica sol gel that serves as a mask for metasurface etching. Similarly, light scattering metagratings may be directly patterned using SCIL in a suitable high-index sol-gel layer.

4.6. Supplementary

4.6.1. Derivation of the design equations

We use the metagrating theory [71] for a periodic array of horizontally oriented magnetic dipoles. The structure is illuminated with a TM-polarized plane wave propagating in the yz plane:

$$\boldsymbol{E}_{inc} = E_0 \left(\boldsymbol{y} \cos(\theta_{inc}) + \boldsymbol{z} \sin(\theta_{inc}) \right) e^{-ik_0(\sin(\theta_{inc})y - \cos(\theta_{inc})z))} \tag{4.4}$$

with E_0 the amplitude, k_0 the free-space wave number and θ_{inc} the angle of incidence. The magnetic dipoles, induced by the incoming wave have each a magnetic current:

$$I_m^x = -i\omega\alpha_m H_{ext}^x \tag{4.5}$$

with H_{ext}^x the impinging magnetic field and α_m the effective magnetic particle polarizability. The dipoles are ordered in a periodic array (m×n) with periodicity d_x and d_y in x and y directions, respectively, and are located at a distance h above a ground plane. The magnetic surface current density $\boldsymbol{J_m}$ is the sum of the currents generated by the discrete magnetic dipole moments:

$$\boldsymbol{J_m}(x,y,z) = \boldsymbol{x} I_m^x \delta(z-h) \sum_{m=-\infty}^{+\infty} \sum_{n=-\infty}^{+\infty} \delta(x - md_x)\delta(y - nd_y) e^{-ik_0 \sin(\theta_{inc}) n d_y} \tag{4.6}$$

The Floquet modes into which the array redirects light are the diffraction orders of the given grating condition. To avoid scattering into higher order modes, we first consider the case of 1D periodicity in the y direction and grating geometries with only three

Floquet modes n=0, ±1 (first-order diffraction above 30°). The radiated field for Floquet mode n is given by:

$$\boldsymbol{E}_n = \left(\boldsymbol{y} - \boldsymbol{z}\frac{k_0\sin(\theta_n)}{k_0\cos(\theta_n)}\right) Q_n \exp(-i\,k_0\sin(\theta_n)\,y - i\,k_0\cos(\theta_n)z) \tag{4.7}$$

with

$$Q_n = \frac{1}{S} I_m^x \cos(k_0\cos(\theta_n)h) \tag{4.8}$$

S is the area of the unit cells ($S = d_y$ for 1D surface). As energy is conserved and no Ohmic dissipation is considered, the extinction power P_{ext} equals the power re-radiated in all Floquet modes:

$$P_{ext} = \frac{1}{2S} Re\{J_m \cdot H_a\} = P_{rad} = \frac{1}{2\eta_0} \sum_{n=-\infty}^{n=+\infty} \frac{1}{\cos\theta_n} |Q_n|^2 \tag{4.9}$$

Employing equation 4.5 and 4.8, 4.9 can be rewritten as:

$$Im\left(\frac{1}{\alpha_m}\right) = \frac{\omega}{\eta_0 d} \sum_{n=-\infty}^{n=+\infty} \frac{1}{\cos\theta_n} \cos^2(k_0 h\cos(\theta_n)) \tag{4.10}$$

In the radiated fields, the field of the n=0 Floquet mode is:

$$\boldsymbol{E}_0 = \left(\boldsymbol{y} - \boldsymbol{z}\frac{k_0\sin(\theta_0)}{k_0\cos(\theta_0)}\right) Q_0 e^{-i\,k_0(\sin(\theta_0)\,y - \cos(\theta_0)\,z)} \tag{4.11}$$

with $Q_0 = \frac{1}{S} I_m^x \cos(k_0 h)$. To cancel the specular reflection of the incident field from the ground plane with the n=0 Floquet mode the condition $E_0 = Q_0$ has to be fulfilled. Combining this condition with the form of the magnetic current from Equation 4.5 gives the condition:

$$\frac{1}{\alpha_m} = \frac{2i\omega}{\eta_0 d} \cos^2(k_0 h) \tag{4.12}$$

Now, we assume that only the 0,-1 and +1 grating orders can carry energy. Comparing equation 4.10 and 4.12 then leads to the design equation for the cancellation of the specular reflection:

$$\cos^2(k_0 h) = \frac{2}{\cos(\theta_1)} \cos^2(k_0 h\cos(\theta_1)) \tag{4.13}$$

This design equation describes which height h of the magnetic dipoles has to be chosen above the ground plane to fully redirect light at normal incidence to the ±1 diffraction orders.

4.6.2. Analytical antenna theory

To implement the metagrating theory into an analytical design structure, we use a method common in antenna theory, and derive the radiation of the total array of magnetic dipoles by summing up the far fields of all individual dipoles. Here, interaction of the dipoles is not taken into account. The far-field radiation by antennas for a magnetic dipole pointing in x direction is given by [80]:

$$E_\theta = i\omega\eta\frac{\epsilon m_x}{4\pi r}e^{-ikr}sin(\varphi) \tag{4.14}$$

$$E_\varphi = i\omega\eta\frac{\epsilon m_x}{4\pi r}e^{-ikr}cos(\theta)cos(\varphi) \tag{4.15}$$

with φ and θ the azimuthal and zenithal angles, respectively. If we consider a 1D geometry (dipoles in a line), $\varphi = \pi/2$, and the electrical field is described by:

$$E_\theta = i\omega\eta\frac{\epsilon m_x}{4\pi r}e^{-ikr} \tag{4.16}$$

Here, ω is the angular frequency, ϵ the permittivity, and μ the permeability ($k_0 = \omega\eta\epsilon$) and m_x is the magnetic moment which takes the form $m_x = \frac{1}{i\omega}SE_0$ due to the condition $E_0 = Q_0$. If the dipole is located above a ground plane with distance h, image theory can be used to describe the far field:

$$E_\theta = E_\theta^+ + E_\theta^- = ik_0 m_x(\frac{1}{4\pi r^+}e^{-ikr^+} + \frac{1}{4\pi r^-}e^{-ikr^-}) \tag{4.17}$$

with r^+ and r^- describing the distance to the dipole located above the ground plane and the image dipole below the ground plane. To calculate the fields in cartesian coordinates r^+ and r^- can be expressed as $r^+ = \sqrt{(y^2 + (z-h)^2)}$ and $r^+ = \sqrt{(y^2 + (z+h)^2)}$. The far field radiation of N_1 dipoles located next to each other at a distance d_1 (on the y axis) is then given by the sum of all individual dipoles and their image dipole:

$$E_{\theta,N_1} = \sum_{n=0}^{n=N_1} E_\theta^+(y - nd_1, z - h_1) + E_\theta^-(y - nd_1, z + h_1) \tag{4.18}$$

Continuing summing of radiated far fields, results in a total far field of all dipoles:

$$E_{tot,N} = \sum_{n=0}^{i=N} E_{\theta,N_i} \tag{4.19}$$

of $N = N_1 + N_2 + ... + N_m$ dipoles with N_1 dipoles with the distance d_1, N_2 dipoles with the distance d_2 and so on.

Based on this derivation, not taking into account the interaction between particles, a design of the far-field scattering of arrays of magnetic dipoles can be made. It should be noted that the scattering towards 0 degree cannot be cancelled mathematically, as here we are considering a finite array, while the design equation 4.13 is based on an infinite plane wave. For this reason, the analytical calculation gives us information about the overall shape of the angular scattering distribution, but not about its efficiency. Figure 4.8 shows the analytically calculated far field for the large-angle reflector metasurface, consisting of 5 magnetic dipoles per metagrating, with optimum height derived from the design equation.

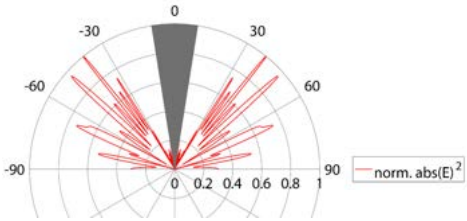

Figure 4.8: Angular profile of far-field intensity analytically calculated from the sum of 25 point dipoles (5 dipoles per angle, 35-75°) and their image dipoles with their respective distances z each obtained from the design equation. The zeroth order scattering contribution is removed (grey zone).

4.6.3. Optimization of structure by simulations

In the following steps, it is shown how we designed the final structure for fabrication. In all steps FDTD Lumerical is used. In all simulations for optimization, periodic boundary conditions were used and metagratings with one fixed period were studies. The structure was illuminated with a plane wave and the power to different grating orders was determined using the grating projection functionality of FDTD Lumerical. We choose to optimize the structure for an operational wavelength of λ = 650 nm, normally incident on a 1D array of Si pillars placed on a Ag substrate with a silica spacing layer. The array has a period of 919 nm (θ_{diff} = 45°). We fix the height z of the pillar to 180 nm. Now, by varying the width w and the distance h between Ag substrate and center of the pillar, we find that at for h = 200 nm and w = 85 nm, almost 50% of the reflected light is scattered towards the +1st order, which given the symmetry, translates to almost 100% diffraction efficiency into the n=±1 modes (Figure 4.9).

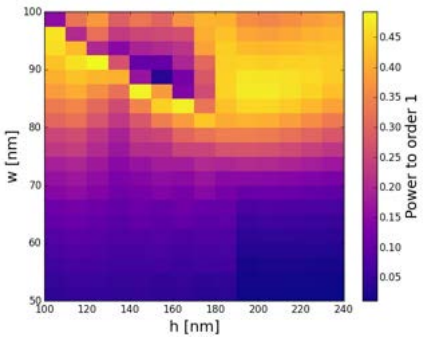

Figure 4.9: Diffraction efficiency into the 1st diffraction order as a function of distance h from particle to the Ag mirror and particle width w.

For ease of fabrication, the distance h was kept constant for all combined metagratings. To investigate the metagrating performance for λ = 650 with periodicities different from 919 nm, we vary the period p as well as the distance h (Figure 4.10). We find that for h = 200 nm for the smaller and bigger periods, up to a pitch of p = 1300 nm (above which the second diffraction order appears) the grating efficiency can be designed to be

above 35% (70% for both n=±1 orders).

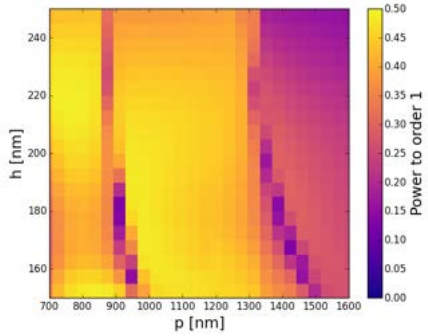

Figure 4.10: Diffraction efficiency into the first diffraction order as a function of array period p and distance h from particle to the Ag mirror.

In fabrication, the width of the individual metagratings can be easily tailored. We investigate how the width of the individual particles affects the performance for different periodicities and find that w = 85 nm gives the best result for all periods (Figure 4.11).

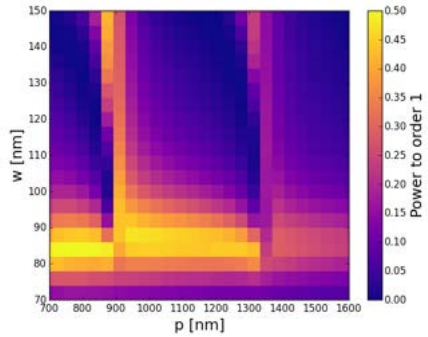

Figure 4.11: Diffraction efficiency into the first diffraction order as a function of array period p and particle width w.

With the chosen parameters (w = 85 nm, z = 180 nm, h = 200 nm), we investigate the effect of varying the array period for the 500-1200 nm spectral range (Figure 4.12). The resonant scattering effect around 650 nm is clearly seen for all periods, and a high coupling efficiency is observed for the bandwidth of the magnetic Mie mode, peaking near 100% on resonance.

As described in the main text, for first-order scattering angles $\theta_{diff} < 30°$ higher-order diffraction complicates the design, that focus on optimizing only the ±1 Floquet modes. As mentioned, we address this problem by modifying the unit cell to contain a number of identical scatterers (3 or 6, depending on the grating pitch) such that their scattering radiation profiles remain within the angular range below 30°. We tune the dis-

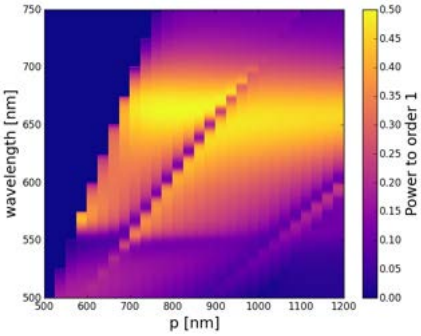

Figure 4.12: Diffraction efficiency into the 1st diffraction order as a function of array period p and wavelength, showing resonant behavior around 650 nm. No diffraction is observed in the dark blue region.

tance between the scatterers to optimize the scattering profile for the highest coupling efficiency towards the first diffraction order. For coupling to the 5°, 15° and 25° angles, we reach efficiencies between 38% and 48% (76% and 96% for both orders) by choosing optimized inter-particle distances of d = 550 nm, 470 nm and 230 nm, respectively (Figure 4.13).

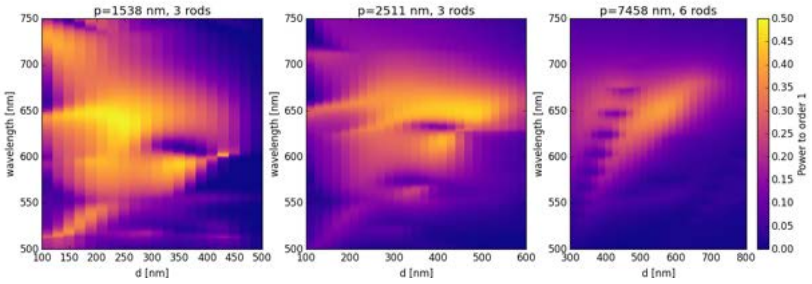

Figure 4.13: Diffraction efficiency into the 1st diffraction order as a function of Si pillar distance d and wavelength for (a) 3 pillars for θ=25° (b) 3 pillars for θ=15° (c) 6 pillars for θ=5°.